

Control of radiation damage in the TEM

R.F. Egerton

Physics Department, University of Alberta, Edmonton, Canada T6G 2G7

ARTICLE INFO

Available online 25 July 2012

ABSTRACT

The problem of electron-beam damage in the transmission electron microscope is reviewed, with an emphasis on radiolysis processes in soft materials and organic specimens. Factors that determine the dose-limited resolution are identified for three different operational modes: bright-field scattering-contrast, phase-contrast and dark-field microscopy. Methods of reducing radiation damage are discussed, including low-dose techniques, cooling or encapsulating the specimen, and the choice of imaging mode, incident-beam diameter and incident-electron energy. Further experiments are suggested as a means of obtaining a better understanding and control of electron-beam damage.

© 2012 Elsevier B.V. All rights reserved.

1. Introduction

Radiation damage provides the main limitation to the spatial resolution of electron-beam imaging or spectroscopy of organic materials. It is also of increasing importance for inorganic specimens (even metals) because of the high current densities obtainable in an aberration-corrected TEM fitted with a field-emission source. In such specimens, high-angle “elastic” (nuclear) scattering can cause knock-on displacement of atoms within a crystalline region, at grain boundaries, or at the surface (electron-induced sputtering). Knock-on displacement of light atoms occurs also in organic samples but the scattering probability and energy deposition are small compared to those arising from the inelastic (electronic) scattering that gives rise to ionization damage (radiolysis).

X-rays are also ionizing radiation and it has recently proved possible to outrun radiation damage by using very short (< 50 fs) pulses. Employing diffractive imaging and iterative phasing, a projected image of a virus was obtained at 32 nm resolution from a single x-ray pulse, while up to a million pulses diffracted from nanocrystals (continuously injected into the beam) yielded a three-dimensional density map of a membrane protein at near-atomic resolution [1,2]. Electrons being charged particles, Coulomb repulsion makes it more difficult to combine short pulses with high spatial resolution, although the diffraction pattern of a 200 μm -wide gold foil has been recorded from a single 100 fs pulse created using velocity bunching [3].

In practice therefore, radiation damage in the TEM remains a problem that cannot be eliminated but may be minimized through various procedures, discussed below. The radiation sensitivity of different specimens varies widely. In conductive

materials, only knock-on (displacement) damage occurs, whereas ionization damage (radiolysis) is of prime importance in semiconductors and insulators, and especially organic specimens that are the main focus of this article.

2. Mechanisms of radiation damage

Knock-on damage arises from the deflection of incident electrons by the electrostatic field of atomic nuclei, the so-called *elastic* scattering that gives rise to diffraction patterns and less than 0.1 eV of energy loss for scattering angles below 100 mrad. The probability of scattering through higher angles is low but the energy transfer may then amount to several eV (sufficient to sputter atoms from a specimen surface) or tens of eV (giving rise to atomic displacement and the formation of defects in crystals). The basics of knock-on damage and methods of avoiding it have been reviewed recently [4].

Ionization damage is a result of the inelastic scattering of electrons. The energy loss E suffered by a primary electron may be transferred to a single atomic electron, which then undergoes a single-electron transition, represented by upward arrows in Fig. 1. Alternatively, the energy E is shared among many electrons in the form of a *plasmon* but this oscillation is rapidly damped, resulting in one or more single-electron transitions.

In the case of a metal, the upward transitions mostly involve conduction-band electrons that are excited to empty states above the Fermi level E_F . This excitation leaves a vacancy (hole) in the valence band, which is filled very rapidly (< 1 fs) because of the high density of conduction electrons. The time-scale associated with atomic vibration being much longer ($\sim 10^{-13}$ s), the atomic nuclei have no time to move before the vacancy is filled [5]. Energy released in the de-excitation process creates numerous phonons (each with energy < 0.1 eV) that represent thermal

E-mail address: regerton@ualberta.ca

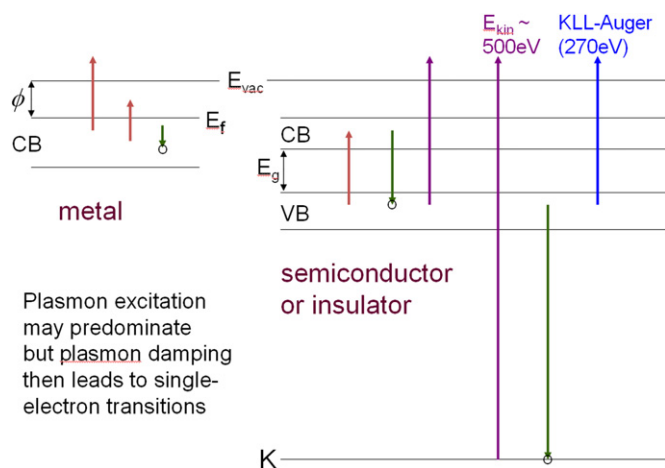


Fig. 1. Energy-band diagram of a metal (on the left) and a semiconductor or insulator (on the right), electron energy being plotted vertically upward. CB and VB represent the conduction and valence bands, ϕ is the work function, E_{vac} , E_f and E_g are the vacuum energy, Fermi energy and CB–VB energy gap. Upward arrows represent single-electron excitations, while downward arrows are de-excitation processes (filling of a VB or K-shell hole). K-shell excitation in an organic material is shown on the right, E_{kin} being the typical kinetic energy of an excited K-shell electron. This process also results in the emission of Auger electrons from the valence band, with an energy of about 270 eV.

vibrations of atomic nuclei (temperature rise) but no permanent displacement of the atoms. In short: the ready supply of electrons prevents radiolytic damage within a metal or a good conductor, such as graphite.

In an insulating or semiconducting specimen, the energy-loss processes are similar but the consequences are different. Single-electron transitions (generated either directly or through plasmons) mostly involve valence electrons excited into the conduction band, generating an electron–hole pair. The average excitation energy $\langle E \rangle$ is several times the energy gap E_g [6] and amounts to 3.7 eV in the case of silicon. Unless produced close to a surface, these excited electrons are *internal* secondary electrons that travel through the specimen and produce further electron–hole pairs before becoming thermalized within about 1 ps [7]. Because of the low electron concentration in the conduction band, a relatively long time elapses before the valence-band hole is filled; minority-carrier lifetimes in semiconductors can be microseconds or more, which greatly exceeds the atomic-vibration period. During this time, the electron wavefunctions may change (stimulated by atomic vibration, for example) and some of the excitation energy becomes as stored as potential energy: there is a change in the interatomic bonding, resulting in the creation of radicals or “broken bonds”.

It takes only a few eV of energy to break a chemical bond, whereas the average energy loss to valence electrons is typically between 20 eV and 30 eV (depending on the material), most of which goes into secondary-electron production. Therefore most of the damage to organic materials comes from secondary electrons, rather than from the primary inelastic event. In poly(methyl methacrylate), it has been estimated that 80% of the damage comes from secondaries [8]. An equivalent situation for x-ray irradiation is that most of the damage is caused by photoelectrons released after the primary absorption event [9].

A further possibility is that inelastic scattering of a primary electron excites an *inner-shell* electron. In the case of carbon, the probability of K-shell excitation is almost a factor of 100 lower than that of valence-electron excitation. However the mean energy loss $\langle E \rangle$ is much higher, so K-shell excitation may account for as much as 30% of the energy exchange (stopping power) in an organic compound [10]. The excited K-electron can

have hundreds of eV of kinetic energy and will itself produce damage by undergoing inelastic collisions. Furthermore, when a valence-band electron fills the core hole, an Auger electron is released with a kinetic energy of 270 eV, creating secondary electrons that produce further damage in the form of bond-breaking. This K-shell mechanism has been proposed as the main cause of damage in *aromatic* compounds [11].

Bond breakage typically results in a loss of short-range order and fading of the diffraction pattern, if the specimen is crystalline. It can also result in radiolytic decomposition (mass loss) and a resulting shrinkage or distortion of the specimen. In biological samples, relatively low doses of radiation cause cell death and enzyme de-activation.

Some inelastic scattering occurs close to the specimen surface and the resulting secondary electrons are emitted into the surrounding vacuum, resulting in a positive space charge within a thin specimen if it is poorly conducting [12]. This charge may deflect the primary beam, causing practical problems in imaging or spectroscopy, or may result in mechanical forces that tear apart the specimen (e.g., a thin film of polymer). The internal electric field can also produce a lateral drift of ions [13], dielectric breakdown or even a Coulomb explosion that results in the electron beam drilling a hole in the specimen [14].

3. Dose-limited resolution

Radiation damage is of particular concern in electron microscopy because of the need for spatial resolution. Otherwise, we could simply defocus the incident beam and spread the damage over a large volume of specimen; the fraction of broken bonds would then become small and radiation damage would cease to be a problem.

In practice, we need information from a small diameter (δ) of the specimen, and in the case of an incident beam of diameter d and current I irradiating a beam-sensitive thin specimen over a time T , the obtainable spatial resolution is limited by the electron fluence or dose $D=IT/d^2$ that the specimen can withstand before the detected signal is degraded. If N electrons are recorded from each resolution element (of area δ^2), the associated shot noise is $N^{1/2}$ and the recorded signal/noise ratio can be defined as

$$\text{SNR} = (\text{DQE})^{1/2} (|\Delta N|/N^{1/2}) = (\text{DQE})^{1/2} (CN/N^{1/2}) = (\text{DQE})^{1/2} CN^{1/2} \quad (1)$$

Here DQE is the detective quantum efficiency of the recording device (square of the actual SNR divided by the square of the ideal SNR); $|\Delta N|=CN$ is the signal, C being the signal/background ratio or contrast between adjacent resolution elements; see Fig. 2.

Radiation damage is determined by the number of electrons incident on the specimen, not the number that reach the detector,

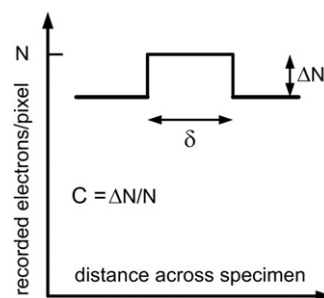


Fig. 2. Recorded signal as a function of distance across the specimen, showing a change ΔN in the number N of recorded electrons per resolution element (size δ), the contrast ratio being defined here as $C=|\Delta N|/N$, so that C is positive even if $|\Delta N|<0$ (negative contrast).

which may be lower by a factor F . In other words, $N = F(D/e)\delta^2$, where D is the electron dose received by the specimen (in Coulomb per unit area), $e = 1.6 \times 10^{-19}$ C is the electron charge, and F is the efficiency of the signal-collection system. For bright-field diffraction-contrast imaging, $F < 1$ because of electron absorption at the objective aperture. For dark-field imaging, the value of F depends on elastic-scattering cross sections, the specimen thickness and the geometry of the detector. For energy-loss spectroscopy, F depends on the inelastic cross sections, specimen thickness and width of the energy-selecting slit (if present).

Substituting for N in Eq. (1) gives an estimate for the dose-limited resolution:

$$\delta = N^{1/2}(FD/e)^{1/2} = (\text{SNR})(\text{DQE})^{-1/2}C^{-1}(FD/e)^{-1/2} \quad (2)$$

To make a high-precision measurement, we would need a large value of SNR and the value of δ would be correspondingly large. However, to simply detect an unknown signal in the presence of noise, SNR=5 is adequate [15,16] and we use this Rose-criterion value in the following discussion.

For a thin specimen and bright-field imaging with a small objective aperture, we might have $F \approx 0.8$, DQE=0.2 (at the Nyquist spatial-frequency limit, for a typical CCD camera and 100 keV electrons), $C=0.1$ (i.e., 10% contrast) and $D=0.01$ C/cm² (typical of the maximum dose needed to degrade an aliphatic compound). In that case, Eq. (2) with SNR=5 gives $\delta \approx 5$ nm, which is typical of the resolution obtainable in a bright-field scattering-contrast image of an unstained polymer. Clearly the spatial resolution obtainable from electron-beam analysis of an organic specimen is considerably worse than that provided by the optics of a modern TEM.

4. Strategies for controlling damage

Radiation damage to a polymer can be highly useful, since it forms the basis of electron-beam and ultraviolet lithography, essential to the microelectronics industry. But in electron microscopy, specimen damage is something to be minimized, particularly when high spatial resolution is desired. As seen from Eq. (2), the dose-limited resolution can be improved by increasing any of the terms DQE, C , F and D .

Employing a recording device with improved DQE is clearly beneficial; CCD cameras and other more recent forms of detector have a DQE that falls below 0.2 at their highest spatial frequency [17]. But even a perfect detector would reduce δ only by a factor of $(0.2)^{-1/2} = 2.2$ and an electron-counting device might fall short of this ideal because of the possibility that two electrons arrive almost simultaneously and are counted as one.

The other factors (C , F and D) are at least partially under the control of the microscopist, and we now discuss procedures for their optimization, starting with the more common techniques and ending with the more controversial.

4.1. Low-dose technique

One obvious way to minimize damage is to avoid pre-irradiating the region of specimen from which data will be recorded. For TEM imaging, software is available to facilitate focusing the image on a nearby area of specimen, then deflecting the incident beam onto the area of interest just before image acquisition starts. For EELS or energy-dispersive x-ray spectroscopy, “smart acquisition” software can be likewise used to control the incident probe [18].

Another standard procedure that is sometimes applicable is to employ multiple copies of the structure being investigated, such as identically-oriented molecules in a molecular crystal, allowing the radiation damage to be spread over all of them. In this way,

the structure of a protein was first determined to 1 nm resolution from electron imaging and diffraction [19]. A similar situation involves proteins or viruses injected within an aqueous jet into a pulsed x-ray beam, although in this case the copies have random orientation and each diffraction pattern must be indexed before the image can be constructed [1,2].

4.2. Maximize the signal

The bright-field image of a biological or polymer specimen, obtained with an on-axis objective aperture, usually exhibits very low contrast. The contrast ratio C is increased by heavy-element staining but this procedure may result in image artifacts and introduces its own resolution limit, typically about 2 nm [20,21]. Higher resolution is possible by using phase contrast, most easily introduced by removing the objective aperture and defocusing the specimen. However, defocusing degrades the image resolution and changes the spatial-frequency content of the image.

A preferable alternative is to keep the specimen in focus and use a phase plate in the back-focal plane of the objective lens [22]. The Boersch phase plate is a miniature electrostatic lens that changes the phase of the central beam relative to that of the scattered electrons [23–25]. The phase shift is varied by adjusting the applied voltage, to allow for different accelerating voltages or to accommodate strong phase objects. A Zernike phase plate consists of a carbon film that retards the phase of scattered electrons and a central hole to allow the undiffracted beam through unaffected. For electrons of wavelength λ and a film of thickness t with a mean inner potential Φ_0 , the phase change is:

$$\varphi = 2\pi(t/\lambda)(e\Phi_0/E_0)[(E_0 + 511\text{keV})/(E_0 + 1022\text{keV})] \quad (3)$$

At an incident energy $E_0 = 100$ keV, about 21 nm of carbon ($\Phi_0 \approx 8$ eV) are needed for $\varphi = \pi/2$, a value often chosen for phase-contrast imaging.

For a TEM fitted with an ideal phase plate (phase shift φ_z) and a very thin specimen whose variation in mean inner potential generates a phase difference $\Delta\varphi$ between adjacent regions, the image contrast is given approximately by the Born-Wolf formula [26]:

$$\Delta N/N = 2 - 2 \cos(\varphi_z) - 2 \cos(\Delta\varphi) + 2 \cos(\varphi_z + \Delta\varphi) \quad (4)$$

For $\varphi_z = \pi/2$, $\Delta N/N = 2 - 2\cos(\Delta\varphi) - 2\sin(\Delta\varphi) \approx -2(\Delta\varphi)$ to within 10% if $\Delta\varphi < 10^\circ$. The contrast is therefore negative (like bright-field scattering contrast) in the sense that denser regions appear brighter in the TEM image, but the ratio $C = |\Delta N|/N$ remains positive according to our definition, increasing up to 0.828 at $\Delta\varphi = 45^\circ$ but then decreasing to zero at $\Delta\varphi = 90^\circ$.

In practice, a phase plate can increase the contrast by a factor of at least 5 relative to a slightly-defocused image of comparable resolution, and image resolution better than 1 nm is possible [22]. Problems associated with contamination and electrostatic charging of the phase plate are reduced by heating it electrically during imaging [27], although a hole-free phase plate that makes use of charging of a carbon film has been demonstrated [28].

Dark-field microscopy also provides high contrast, for example using a STEM and high-angle dark-field (HAADF) detector [29]. However, the HAADF signal is weak because of the relatively small cross sections for high-angle scattering, equivalent to a small value of F in Eq. (2). We re-examine this situation in Section 4.7.

Table 1 gives estimates of the contrast and resolution for 100 keV electrons in the three different TEM imaging modes: bright-field TEM with 10 mrad objective aperture, TEM with an ideal phase plate (90° phase shift, cut-on frequency = 0, negligible phase-plate scattering) and STEM with an annular dark-field detector with 10 mrad inner angle. The angular distributions of

Table 1

Calculated contrast and resolution in three imaging modes (bright-field TEM with 10 mrad objective aperture, ideal phase plate, ADF-STEM with 10 mrad inner angle) for 100 keV electrons and a polymer ($Z=6$, density=1 g/cm³, $\Phi_0=6$ eV) with a 10% density change. The dose-limited resolution is for SNR=5, DQE=1 and $D=0.01$ C/cm².

Imaging technique	Contrast C($t=10$ nm) (%)	Contrast C($t=100$ nm) (%)	Resolution $\delta(t=10$ nm)	Resolution $\delta(t=100$ nm)
BF-TEM	0.4	4	48 nm	6 nm
Phase plate	11	75	2 nm	0.3 nm
ADF-STEM	9	7	10 nm	5 nm

Table 2

Typical values of the characteristic dose D_c and cross section σ_d for damage to organic materials from 100 keV electrons, deduced from fading of the diffraction pattern [33], decrease in low-loss fine structure [34] and mass-loss measurements [34].

Measurement	Material	D_c (C/cm ²)	σ_d (Mbarn)
Electron diffraction	C ₂₆ paraffin	0.007	23
	Anthracene (C ₁₄ H ₁₀)	0.01	16
	Phthalocyanine(C ₃₂ H ₁₈ N ₈)	0.2	0.8
	Cu-phthalocyanine	2.5	0.06
	Chlorinated Cu-phth	30	0.005
Low-loss EELS	Aliphatic	0.05	3.2
	Aromatic	0.3	0.56
Total mass loss	Aliphatic	0.006	27
	Aliphatic/aromatic	0.02	8
	Aromatic	2	0.1

elastic and inelastic scattering were taken from a Lenz model, as described in Section 4.7. Contrast values are for 10% density change in a polymer with density=1 g/cm³, effective atomic number=6 and mean inner potential of 6 eV [30,31]. The dose-limited resolution was estimated from Eq. (2) with SNR=5, DQE=1 and $D=0.01$ C/cm². Although the ideal phase plate assumed here does not currently exist, the potential advantages of this concept (in terms of enhanced contrast and resolution) can be seen.

When carrying out electron energy-loss spectroscopy (EELS) in a TEM, the value of F is increased and the available resolution is improved by avoiding the use an energy-selecting slit. This means using parallel (rather than serial) recording of the spectrum and STEM (rather than EFTEM) for spectrum-imaging. Energy-filtered imaging can be used in several different ways, some of which provide valuable chemical contrast [32].

In addition to optimizing the measurement process, the dose-limited resolution δ would be further improved if the radiation dose D could be increased. To avoid degrading the specimen, we need to increase its critical or characteristic dose D_c , defined as the dose (C/cm²) at which the measured signal becomes seriously corrupted according to some specified criterion. For example, it may be the dose at which inner diffraction spots (from a crystalline specimen) decrease in intensity by a factor of $e=2.718$, or an energy-loss peak decreases by this same factor. Table 2 gives some rough estimates of critical dose for various kinds of organic material, measured in different ways and all scaled to an incident energy of 100 keV.

Whereas D_c is measure of radiation resistance of the specimen, the damage cross section $\sigma_d=e/D_c$ (where $e=1.6 \times 10^{-19}$ is the electron charge) is a measure of its radiation sensitivity. If σ_d approaches 2 Mbarn ($=2 \times 10^{-18}$ cm², the total-inelastic cross section for a carbon atom for 100 keV electrons), it takes on average about one inelastic excitation per atom to cause damage in the specimen. If σ_d becomes as high as $2n$ Mbarn, where n is the

number of carbon atoms per molecule, only one excitation per molecule is sufficient to cause damage, a situation approached in the more sensitive aliphatic compounds; see Table 2.

Although characteristic of the material of the specimen, the values of D_c and σ_d may depend also on factors that are within experimental control: specimen preparation, specimen temperature during the microscopy, incident-beam current and diameter, and TEM accelerating voltage. These factors are considered in turn in the remainder of this article.

4.3. Cool the specimen

Reducing the specimen temperature is sometimes thought of as counteracting the heating effect of the electron beam but this interpretation is inadequate, radiation damage being a process distinct from thermal decomposition. In any event, the heating effect is small if the beam current I is low, which is the case for an electron probe of small diameter d . Assuming heat is conducted away over a radial distance R_0 , the temperature rise is:

$$\Delta T \approx \langle E \rangle (2R_0/d) / (4\pi\kappa\lambda_i) \quad (5)$$

where $\langle E \rangle$ is the mean energy loss (in eV) per inelastic-scattering event, λ_i is the inelastic mean free path of the transmitted electrons and κ is the thermal conductivity of the specimen. For $I=1$ nA, $R_0=30$ μ m (typical distance to a grid bar) and specimen parameters ($\kappa=1.6$ W m⁻¹ K⁻¹, $\lambda_i=150$ nm, $\langle E \rangle \approx 40$ eV) appropriate to carbon and 200 keV electrons, $\Delta T \approx 0.05$ K for $d=1$ μ m. Because the radial heat flow results in a logarithmic d -dependence, the temperature rise only increases to 0.15 K for a 1 nm-diameter probe, despite the high current density (10^5 A cm⁻²).

Thermal effects do become important if the beam current approaches 1 μ A, even for large-diameter (e.g., 100 μ m) illumination, and especially for polymers whose thermal conductivity can be as low as 0.24 W m⁻¹ K⁻¹ [35].

Even in the absence of significant beam heating, there is substantial evidence that lowering the specimen temperature increases the characteristic dose D_c and decreases the radiation sensitivity. For example, TEM measurements in several laboratories (Duke University, EMBL, Siemens Corp., Zemlin and Heide groups) of fading of the electron-diffraction pattern of 5.8 nm paraffin films showed that the critical dose increased by a factor of 3 to 4 after a specimen was cooled from room temperature to 100 K [36]. A further small increase (variable between different labs) was reported when the specimen was cooled to 10 K. These diffraction measurements relate to the destruction of short-range order in a crystalline organic specimen. The outer diffraction spots fade first, as they represent higher spatial frequency and are more sensitive to atomic displacement, but D_c is usually defined as the dose that eliminates all the diffraction spots.

Mass-loss measurements often show a larger increase in critical dose with cooling, as illustrated in Table 3. In these measurements, the characteristic dose is measured as the dose that reduces the concentration of a given element by a factor of $e=2.718$. The temperature dependence of D_c is greater for less stable (more radiation-sensitive) materials and for removal of gaseous elements. Such results are usually interpreted as a “freezing in” of volatile elements, reflecting the low diffusion rate at low temperature. Consequently, the cryoprotection is only temporary; volatile elements are released from the irradiated area when the specimen returns to room temperature [37].

4.4. Modify the specimen

As seen in Table 4, replacing the hydrogen in an organic compound by a halogen is found to reduce the radiation

Table 3

Factor by which the characteristic dose for removal of a specified element increases when the sample is cooled from 300 K to 100 K, as measured by core-loss spectroscopy [38].

Specimen	Element removed	D_c (300 K)C/cm ²	(100 K/300 K) D_c ratio
Nitrocellulose	N	0.002	120
Nitrocellulose	O	0.006	90
Nitrocellulose	C	0.06	5
Poly(vinyl formal)	O	0.03	30
Poly(methyl methacrylate)	O	0.06	8
Poly(methyl methacrylate)	C	0.5	1.6
Polycarbonate	O	0.5	> 10
Carrageenan	O	0.05	20
Carrageenan	C	0.08	12
Chlorinated CuPhthalocyanine	Cl	3	3

Table 4

Critical dose D_c for the destruction of lattice fringes in crystalline aromatic films supported on thin carbon (with and without a 10 nm carbon covering film) and in crystalline paraffin (with and without a SiO coating) [42].

Specimen material	Thickness (nm)	D_c (uncoated) (C/cm ²)	D_c (coated) (C/cm ²)
Perylene (C ₂₀ H ₁₂)	7	0.024	0.07
	33	0.04	0.11
Metal-free Phthalocyanine (C ₃₂ H ₁₈ N ₈)	8	0.17	0.49
	13	0.73	1.6
	20	1.9	2.7
Chlorinated Cu Phthalocyanine	5.4	2.1	19.5
	10.3	6.3	29
Paraffin (C ₃₆ H ₇₄)	Unknown	0.00024	0.0073
	Unknown	0.00036	0.0095

sensitivity, probably due to an atomic “cage effect” (steric hindrance of the larger halogen atoms). In favorable cases, such substitution leaves the chemical properties and structure of the specimen unchanged. Table 4 also illustrates the fact that aromatic compounds are generally less radiation sensitive than aliphatic ones (such as paraffins), a property attributed to the resonance stabilization of the phenyl rings [39].

Encapsulating a thin-film organic specimen on both sides with a metal, carbon or SiO layer is also reported to increase the critical dose, for both mass loss [38] and loss of crystallinity [40–42]; see Table 4.

A conductive coating will likely reduce the electrostatic charging of an insulating specimen and might act as a source of electrons, increasing the recombination rate (Fig. 1). However, an insulating covering of SiO was found to be equally effective [42]. Another possibility is that the coating acts as a diffusion barrier that retains mobile species within the specimen, preventing mass loss and even structural damage. In support of the latter argument, Fryer and Holland [41] reported that the protection factor is less for thicker films, suggesting that the sample acts as its own protectant. Indeed, their measured characteristic dose for damage to uncoated specimens increased with specimen thickness (Table 4).

When damage occurs at the surface, as in electron-induced sputtering, a carbon coating offers temporary protection (as a sacrificial layer) until it is sputtered away [43]. Carbon-contamination layers formed by electron-beam polymerization of surface hydrocarbons are non-conducting but could act as both a

diffusion and a sputtering barrier; a 10 nm contamination layer prevented electron-beam sputtering of Ni₃Al during one hour of observation [44]. A similar improvement in radiation stability was obtained by encapsulating metal atoms in C₆₀ molecules inside a carbon nanotube [45]. In this case, damage implies the displacement or ejection of the metal atoms, probably by the knock-on process.

Electron-beam damage to metal oxides may involve surface desorption induced by electronic transitions (DIET) [46,47]. Covering TiO₂ with a graphitic carbon layer has been reported to slow down the formation of a highly-defective (almost amorphous) surface layer by a factor of more than 200 [48].

4.5. Reduce the incident intensity

Reducing the incident-beam current lengthens the time needed to record an image or spectrum, increasing the likelihood of specimen, electron-beam or high-voltage drift. However, it ensures that radiolysis will not be enhanced as a result of beam heating and it reduces the risk of thermal decomposition or electrostatic-charging effects. Charging of an insulating specimen creates an external electric field that can deflect the incident beam or generate mechanical forces that destroy the specimen (polymers for example). Because the primary electrons pass through a thin specimen without absorption and secondary electrons are emitted from both surfaces, an insulating TEM specimen develops a positive charge at typical incident-electron energies.

Charging effects may exhibit a threshold incident intensity (current density), below which no damage occurs, as noted for inorganic oxides [49] and modeled by Cazaux [14]. This is one example of a dose-rate effect, in which the damage depends on current density (dose rate) as well as on accumulated dose. At the low current densities possible for organic specimens, the dose-rate effects appear to be negligible [38,10].

If the radiation sensitivity gradually increases with increasing current density, the effect is explainable in terms of beam heating and the consequent reduction in D_c [50,51]. However, the opposite trend was reported by Fryer [52], who recorded lattice images of monolayer aromatic films (e.g., acetyl pyrene) using a high dose rate and short recording times (10–100 ms), the accumulated dose (≈ 0.16 C/cm²) being thirty times larger than the dose that removed low-order diffraction spots at low incident intensity. Damage might be avoided entirely if an adequate number of electrons could be delivered in less than 50 fs [53].

An interesting observation is that damage to some organic films occurs first at the edges, creating amorphous regions that grow inwards to replace the original crystalline regions [54,55]. More observations or modeling of this effect would be useful.

4.6. Reduce the incident-beam diameter

Downing and Glaeser [56] obtained higher contrast in HREM images of paraffin and purple membrane after reducing the illumination diameter from 3 μ m to below 100 nm, with lower beam current. The cause was found to be specimen movement due to radiation-induced shrinkage of the films. A spot-scan method was then used to gather data from a larger area [57]. Later studies [58] found that monolayer paraffin specimens supported on thick (35 nm) rather than thin (13 nm) carbon had improved mechanical stability, giving an image contrast as high as that expected from the electron-diffraction pattern.

Measurements on various polymers have shown an unexpected effect of probe diameter. The characteristic dose for fading of the 7 eV peak in the energy-loss spectrum (indicative of phenyl rings) increased by several orders of magnitude as the electron-beam

diameter was reduced from 1 μm to 1 nm [10,59,60]. One proposed explanation is that much of the damage is produced by secondary electrons, a larger fraction of which deposit their energy outside the probe when the diameter is small. Digital-linescan measurements confirm that damage is produced several nm outside the probe [59,10]. Although the range of fast secondaries (those with starting energies above 50 eV) can extend to several tens of nm, there does not appear to be a sufficient number of them to account for a large change in D_c . A further complication is that energy-loss information is extracted from regions of specimen outside the probe, due to the delocalization of inelastic scattering; in the case of a low-loss (7 eV) peak, this delocalization extends to nearly 30 nm [10]. In any event, it is not clear that a small-diameter probe can be used to extract any more information from the polymer in relation to the damage produced.

4.7. Change the incident energy

Where damage arises from a knock-on mechanism, as in graphene or carbon nanotubes for example, lowering the incident-electron energy below about twice the displacement threshold results in less damage, and reducing it below the threshold may avoid damage entirely [4,61]. In the case of ionization damage, the reverse is true because the cross section σ_i for inelastic scattering varies inversely with the primary energy E_0 , the damage cross section σ_d being higher at low incident energy. However, the inelastic signal (used in EELS and x-ray emission spectroscopy) increases by the same factor, and the elastic signal (giving TEM contrast) by a similar factor. Therefore the signal/damage ratio might be expected to be independent of incident energy.

In support of the above conclusion: an inverse proportionality between σ_i and E_0 is predicted by the Bethe theory of inelastic scattering [62], while the proportionality of σ_i and σ_d is in accord with the assumption that damage is proportional to the energy deposited through inelastic scattering. The resulting proportionality of σ_d and D_c has been verified for incident energies between 30 keV and 300 keV [34,51].

At very low incident energies, these assumptions have been questioned. Aromatic samples irradiated in a scanning electron microscope, followed by TEM measurements of diffraction-pattern fading on the same area of specimen, suggested a

reduction in damage cross section for irradiation energies below about 1 keV [63]. Above 30 keV, the damage cross sections *per molecule* are comparable to the K-shell inelastic cross section for one carbon atom [64], suggesting that a single K-excitation (per molecule) might be sufficient to destroy the structure of resonance-stabilized aromatic compounds [39]. The reduction in σ_d below 1 keV could then be interpreted as being due to reduction in the K-shell cross section, resulting in zero damage for incident energies below the K-shell ionization threshold (285 eV).

The above measurements were complicated by the fact that the electron range becomes very small (65 nm or less) below 1 keV, leading to the possibility that low-energy irradiation damages only the surface of a specimen, leaving undamaged material that is detected by subsequent TEM diffraction. Recognizing this problem, Stevens et al. [65] performed their diffraction measurements in the same instrument and reported that the damage cross section for an aromatic compound (coronene) fell by a factor of 3.8 from 300 eV to 250 eV (below the carbon K-threshold), whereas this factor was only 2.8 for an aliphatic compound (tetracontane). The damage cross sections themselves fall with decreasing incident energy because the electron stopping power falls for $E_0 < 1$ keV. Subsequent SEM measurements of the radiation-induced fading of cathodoluminescence failed to detect any threshold behavior for that type of damage, the damage rate being proportional to the deposited energy [64].

Even in the *absence* of threshold effects, such that the signal/damage ratio is independent of incident energy, the dose-limited resolution δ is not necessarily independent of accelerating voltage; its behaviour depends on the measurement mode. To illustrate this, we assume no change in DQE with E_0 , in which case Eq. (2) predicts

$$\delta \propto C^{-1} F^{-1/2} D_c^{-1/2} \propto C^{-1} F^{-1/2} \sigma_d^{1/2} \quad (6)$$

We first apply this formula to *bright-field scattering contrast* in a TEM with a thin amorphous specimen of thickness t , ignoring any change in D_c due to electron-beam heating effects that could be significant for more radiation-resistant aromatic materials [51]. We assume that the objective aperture intercepts most of the electrons that are scattered elastically (with mean free path λ_e), while transmitting most of those that are scattered inelastically. The aperture collection efficiency is then $F \approx \exp(-t/\lambda_e) \approx 1$ for small thickness t . Non-relativistically, the elastic-scattering

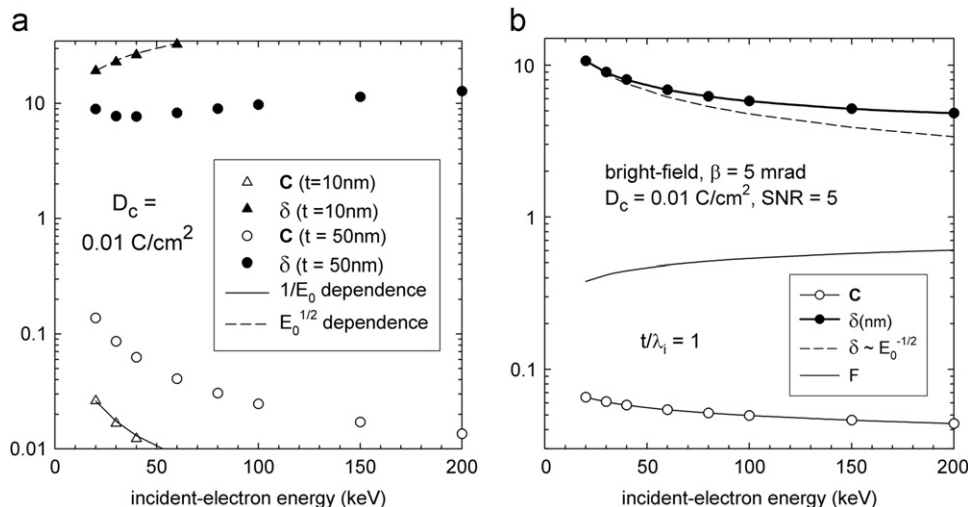


Fig. 3. Bright-field contrast C , dose-limited resolution δ and fraction F of electrons that pass through a 5 mrad objective aperture, calculated using the LenzPlus.m program [66], for a 10% density change in an amorphous aliphatic specimen ($D_c = 0.01 \text{ C}/\text{cm}^2$). For an aromatic material with $D_c = 1 \text{ C}/\text{cm}^2$, the values of δ would be a factor of 10 lower. In (a), we assume constant specimen thickness; in (b), the specimen thickness t is scaled proportional to the inelastic mean free path.

cross section is $\sigma_e \propto \sigma_d \propto 1/E_0$, giving $C \propto \Delta N \propto \sigma_e t \propto E_0^{-1} t$ for small t and $\delta \propto t^{-1} \sigma_e^{-1} \sigma_d^{1/2} \propto t^{-1} E_0^{1/2}$. For a given specimen thickness, the resolution gets better (smaller δ) as E_0 is reduced (due to a stronger elastic signal and despite an increase in radiation sensitivity), in agreement with measurements on copper phthalocyanine [51].

To provide a more accurate prediction, we can apply correct relativistic scaling for σ_e and σ_d and use the Lenz model together with the Poisson formula for plural scattering to calculate the fraction F of elastic and inelastic scattering passing through the aperture [66]. As shown in Fig. 3a, the E_0 -dependences for C and δ predicted above hold (at low E_0) for a 10 nm specimen, whereas for a 50 nm specimen the dose-limited resolution is nearly independent of thickness.

Assuming equal specimen thickness for all E_0 may be somewhat unrealistic; at low incident energy, electron scattering is stronger, leading to a low-intensity TEM image (low value of F) and greater loss of resolution due to chromatic aberration. So in practice, thinner specimens are required at low incident energy. If we scale t in proportion to the elastic or inelastic mean free path ($\propto E_0$), the objective aperture should transmit a similar fraction F of the electrons. Then C becomes constant and $\delta \propto E_0^{-1/2}$ according to Eq. (6), the resolution becoming worse at low incident energy. As shown in Fig. 3b, calculations that include relativistic kinetics and plural scattering support this conclusion but above 100 keV the dose-limited resolution changes little.

Phase contrast offers the possibility of higher resolution, especially if TEM phase plates can be improved, as mentioned in Section 4.2. For a thin amorphous specimen, we can again make rough predictions of the effect of lowering the incident energy E_0 by using non-relativistic formulas, neglecting inelastic and plural scattering and using a weak-phase-object approximation. According to Eq. (3), the difference in phase shift between different regions of the specimen is $\Delta\phi \propto (t/\lambda)E_0^{-1} \propto t E_0^{-1/2}$, and from Eq. (4) the resulting phase contrast is $C \propto \Delta\phi \propto E_0^{-1/2}$ for a fixed specimen thickness t . Then according to Eq. (2), $\delta \propto C^{-1} D_c^{-1/2} \propto E_0^{1/2} E_0^{-1/2} = \text{constant}$. But at low E_0 , amplitude contrast ($\propto E_0$ for low t) increases in relative importance and adds constructively (in phase), improving the contrast and resolution if chromatic and spherical aberrations are corrected [67]. If we keep t/λ_i constant, the amplitude component remains low, $C \approx \lambda_i E_0^{-1/2} \approx E_0^{1/2}$ and $\delta \propto 1/E_0$, the resolution becoming worse at lower incident energy.

To derive quantitative estimates of phase contrast and resolution, we applied Eq. (3) and Eq. (4) to an amorphous organic material (effective $Z=6$, density = 1 g/cm³) containing a 10% step in mean atomic potential. The characteristic dose was scaled according to the square of the incident velocity v , relativistically more correct than scaling proportional to E_0 . The results, shown in Fig. 4, confirm that higher incident energy favours high resolution, 2 nm being possible in a thin specimen of a typical aliphatic material ($D_c \approx 0.01$ C/cm²) and 0.2 nm for a beam-resistant aromatic specimen ($D_c \approx 1$ C/cm²).

Dark-field imaging of a very thin specimen gives a material-contrast ratio C , due to variations in atomic number for example, that is independent of specimen thickness. But $F \propto t \sigma_e$, giving $\delta \propto (t)^{-1/2} (\sigma_d/\sigma_e)^{1/2}$. The dose-limited resolution is therefore independent of accelerating voltage for a fixed value of t , or else $\delta \propto E_0^{-1/2}$ if the thickness is scaled proportional to E_0 .

In Fig. 5, the case of ADF-STEM imaging is simulated for a 10% change in atomic number within an amorphous organic material (effective $Z=6$, density = 1 g/cm³). The angular distribution of elastic and inelastic scattering was taken from the Lenz atomic model, making allowance for plural scattering and broadening of the angular distributions with increasing order of scattering [66]. We assumed that the outer angle of the ADF detector was several times that of the inner angle β , so that nearly all electrons

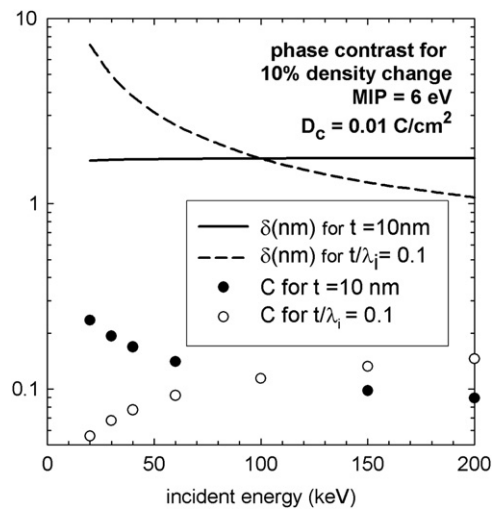


Fig. 4. Phase contrast C and dose-limited resolution δ for a 10% change of mean inner potential within an organic specimen ($\phi \approx 6$ eV), calculated from Eqs. (2)–(4) assuming an ideal $\pi/2$ phase plate. The calculations assume $D_c = 0.01$ C/cm²; values of δ would be a factor of 10 lower for $D_c = 1$ C/cm², typical of some aromatic compounds.

scattered through angles greater than β are collected. Making use of Eq. (2), the dose-limited resolution δ is given by:

$$\delta^2 = (\text{SNR})^2 P_1 (D/e)^{-1} (P_2 - P_1)^{-2} \\ = (4 \times 10^{-4}) P_1 [D_c (T/76.8 \text{ keV})]^{-1} (P_2 - P_1)^{-2} \quad (7)$$

where P_1 is the probability of (elastic and/or inelastic) scattering through an angle greater than β , P_2 is the equivalent probability for a material with atomic number (and mean energy loss) 10% higher, and D_c is the critical dose at $E_0 = 100$ keV ($T = mv^2/2 = 76.8$ keV).

As seen in Fig. 5a, $\delta(\beta)$ has a broad minimum: the optimum ADF inner angle β^* depends on specimen thickness and incident energy but lies within the range 10–50 mrad. As β is increased above β^* , the ADF collection efficiency and signal ($P_2 - P_1$) decrease, giving larger δ . For $\beta < \beta^*$, there is little or no increase in ($P_2 - P_1$) but an increase in P_1 , resulting in an increase in statistical noise and higher δ . For $E_0 = 100$ keV and a specimen thickness t equal to the inelastic mean free path ($\lambda_i \approx 100$ nm), the optimum resolution is $\delta^* \approx 4$ nm (with $\beta^* \approx 4$ mrad). For 30 keV and $t = \lambda_i \approx 35$ nm, the optimum resolution is about 6.5 nm (at $\beta^* \approx 40$ mrad). For a thinner specimen (e.g., $t/\lambda_i \approx 0.1$, hollow data points in Fig. 4a), values of δ are larger because of the smaller ADF signal. In the case of a typical aromatic material with $D_c \approx 1$ C/cm² at 100 keV, all values of δ would be a factor of 10 smaller, as predicted by Eq. (2).

The dependence of the optimized ($\beta = \beta^*$) resolution on specimen thickness is shown in Fig. 5b.

The value of δ^* falls with increasing thickness because of the larger ADF signal. For sufficiently thick specimens, however, the resolution should deteriorate by an amount x_0 because of spreading of the probe due to elastic scattering, given approximately by [35]:

$$x_0 (\text{nm}) = 0.0332 (\rho A)^{1/2} [Z/E_0] [(1 + E_0/511)/(1 + E_0/1022)] t (\text{nm})^{3/2} \quad (8)$$

where the density ρ is in g/cm³, A is the atomic weight and E_0 is in keV. Despite this broadening, Fig. 5b suggests that 5 nm resolution, useful for some purposes, can be obtained in relatively thick beam-sensitive specimens ($t \approx 4\lambda_i \approx 145$ nm) using ADF-STEM at $E_0 = 30$ keV.

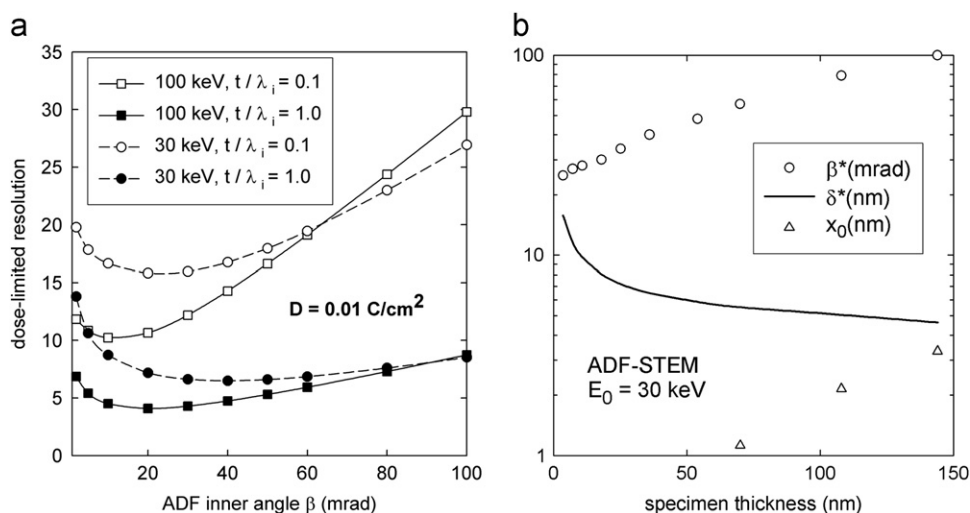


Fig. 5. Calculations of the STEM-ADF dose-limited resolution δ for 10% density change in an amorphous aliphatic material ($D_c = 0.01 \text{ C/cm}^2$ at 100 keV) based on the LenzPlus.m program [66] and Eq. (2) with $\text{SNR} = 5$, $\text{DQE} = 1$. (a) Dependence of δ on ADF inner angle β ; values would be a factor of 10 lower for an aromatic material with $D_c = 1 \text{ C/cm}^2$ (at 100 keV). (b) Thickness dependence of the optimum resolution δ^* at $E_0 = 30 \text{ keV}$, together with estimates of the exit-surface beam broadening x_0 .

As remarked previously, the effect of changing the incident energy is different if the mechanism of radiation damage is predominantly knock-on displacement. In a simple case (e.g., monatomic solid), the displacement cross section decreases when the incident energy falls below about twice the threshold energy, becoming zero below the threshold energy. Kaiser et al. [68] found that visible damage to C_{60} molecules embedded in a double-walled carbon nanotube required about 100 times more electron dose at 20 keV compared to 80 keV, where the damage dose was about 160 C/cm^2 .

If radiation damage to the specimen is absent, the image-acquisition time can in principle be increased until electron-beam shot noise becomes low enough that the resolution is determined by other factors such as specimen drift, electron optics, chromatic aberration and beam spreading (in a thicker specimen). ADF-STEM images of multi-walled carbon nanotubes, with high contrast and resolution better than 2 nm, have been obtained using a SEM operating with 5 kV accelerating potential [69], well below the threshold for knock-on damage.

5. Conclusions and future experiments.

Although the broad principles of radiation damage are understood, many practical questions remain unanswered. It would be satisfying and even useful if the damage process of a simple organic compound could be simulated by quantum-mechanical calculations, taking into account atomic motion. Among other things, such a calculation might predict the temperature dependence of damage (for comparison with experiment) and the effect of elemental substitution, for example of hydrogen by heavier elements.

The high radiation sensitivity of organic materials usually limits the image resolution obtainable in TEM, rather than instrumental performance. Radiation damage to a crystalline specimen results in mechanical distortion that can cause the image resolution to be substantially worse than that expected from the electron-diffraction pattern. Measures to prevent this include small-spot scanning and using a thicker support film.

Cooling the specimen to liquid-nitrogen temperature gives a useful increase in radiation resistance, sometimes by as much as a factor of 10. There is evidence that encapsulating a specimen (e.g.,

covering a thin film on both sides with evaporated carbon) also decreases its radiation sensitivity. The mechanism is not firmly established and further exploratory work is needed to investigate the encapsulation of both organic and inorganic specimens, together with the possible dependence of radiation sensitivity on specimen thickness.

Unlike inorganic materials, dose-rate effects in organic specimens appear to be small at the low current densities conventionally used for image recording. Further experiments are desirable to find out if a higher information/damage ratio can be obtained by using a short recording time. Electron sources are being developed to allow time resolution in the sub-ps region and it will be interesting to see if they can be applied to TEM studies of beam-sensitive materials.

Simulations based on simple models of scattering suggest that reducing the incident energy improves the dose-limited resolution only if the damage arises from knock-on displacement (high-angle elastic scattering). It is possible that more elaborate calculations would indicate otherwise, and quantitative measurements at incident energies below 60 keV are highly desirable. In addition to electron imaging, electron diffraction and EELS can provide valuable insight into the damage process and its dependence on parameters such as incident energy.

The simple calculations presented here illustrate the possibility of achieving sub-nm resolution in beam-sensitive specimens, using phase-contrast imaging. However, the role of various imaging modes should be further explored, including methods of extracting phase-contrast information in STEM mode. For fixed-beam TEM, the practical situation will be improved if phase plates can be developed that are immune to damage and contamination, with a low cut-on frequency that provides high contrast [67,70].

Acknowledgments

The author is grateful for valuable discussions with Matt Libera, Harald Rose, Bob Glaeser, Dirk Van Dyck, Fu-Rong Chen, Marco Beleggia and Marek Malac, and for financial support from the National Science and Engineering Research Council of Canada.

References

- [1] H.N. Chapman, et al., *Nature* 470 (2011) 73.
- [2] M.M. Seibert, et al., *Nature* 470 (2011) 78.
- [3] T. van Oudheusden, P.L.E.M. Pasmans, S.B. van der Geer, M.J. de Loos, M.J. van der Wiel, O.J. Luiten., *Physical Review Letters* 105 (2010) 264801.
- [4] R.F. Egerton, R. McLeod, F. Wang, M. Malac, *Ultramicroscopy* 110 (2010) 991.
- [5] L.W. Hobbs, *Ultramicroscopy* 3 (1979) 381.
- [6] W. Shockley, *Czechoslovak Journal of Physics* 11 (1961) 81.
- [7] C.R. Arumainaya, H.-L. Lee, R.B. Nelson, D.R. Haines, R.P. Gunawardane, *Surface Science Reports* 65 (2010) 1.
- [8] B. Wu, Neureuther, *Journal of Vacuum Science & Technology B* 19 (2001) 2508.
- [9] C. Nave, M.A. Hill, *Journal of Synchrotron Radiation* 12 (2005) 299.
- [10] R.F. Egerton, S. Lazar, M. Libera, *Micron* 43 (2012) 2.
- [11] M.S. Isaacson, *Principles and Techniques of Electron Microscopy*, 7, in: M.A. Hayat (Ed.), Van Nostrand, New York, 1973.
- [12] L. Reimer, U. Golla, B. Roengeler, M. Kaessens, B. Schindler, R. Senkel, *Optik* 92 (1992) 14.
- [13] N. Jiang, J. Silcox, *Journal of Applied Physics* 92 (2002) 2310.
- [14] J. Cazaux, *Ultramicroscopy* 60 (1995) 411.
- [15] A. Rose, *Advances in Electronics* 1 (1948) 131.
- [16] M.K.H. Natusch, C.J. Humphreys, N. Menon, O.L. Krivanek, *Micron* 30 (1999) 173.
- [17] G. McMullan, S. Chen, R. Henderson, A.R. Faruqi, *Ultramicroscopy* 109 (2009) 1126.
- [18] K. Sader, B. Schaffer, G. Vaughan, R. Brydson, A. Brown, A. Bleloch, *Ultramicroscopy* 110 (2010) 998.
- [19] P.N.T. Unwin, R. Henderson, *Journal of Molecular Biology* 94 (1975) 425.
- [20] R. Henderson, *Ultramicroscopy* 46 (1992) 1.
- [21] T.M. Chou, P. Pravoonthong, A. Aitouchen, M. Libera, *Polymer* 43 (2002) 2085.
- [22] K. Nagayama, *Journal of Microscopy* 60 (supplement 1) (2011) S43.
- [23] K.-F. Chen, C.-S. Chang, J. Shiue, Y. Hwu, W.-H. Chang, J.-J. Kai, F.-R. Chen, *Micron* 39 (2008) 749.
- [24] R. Cambie, K.H. Downing, D. Typkeb, R.M. Glaeser, J. Jina, *Ultramicroscopy* 107 (2007) 329.
- [25] D. Alloyeau, W.K. Hsieh, E.H. Anderson, L. Hilken, G. Benner, X. Meng, F.R. Chen, C. Kisielowski, *Ultramicroscopy* 110 (2010) 563.
- [26] M. Beleggia, *Ultramicroscopy* 108 (2008) 953.
- [27] R. Danev, R.M. Glaeser, K. Nagayama, *Ultramicroscopy* 109 (2009) 312.
- [28] M. Malac, M. Beleggia, M. Kawasaki, P. Li, R.F. Egerton, *Ultramicroscopy* 118 (2012) 77.
- [29] E. Sourty, S. van Bavel, K. Lu, R. Guerra, G. Bar, J. Loos, *Microscopy and Microanalysis* 15 (2009) 251.
- [30] R.R. Lunt, S. Kena-Cohen, J.B. Benziger, S.R. Forrest, *Physical Review Letters* 102 (2009) 065504.
- [31] Y.C. Wang, T.M. Chou, M. Libera, E. Voekl, B.G. Frost, *Microscopy and Microanalysis* 4 (1998) 146.
- [32] M.R. Libera, R.F. Egerton, *Polymer Reviews* 50 (2010) 321.
- [33] L. Reimer, *Physical Aspects of Electron Microscopy and Microbeam Analysis*, in: B.M. Siegel, D.R. Beaman (Eds.), Wiley, New York, 1975.
- [34] M. Isaacson, *Ultramicroscopy* 4 (1979) 193.
- [35] L. Reimer and H. Kohl, *Transmission Electron Microscopy* (Springer, New York, 2008).
- [36] International Experimental Study Group, *J. Microscopy* 141 (1986) 385.
- [37] R.F. Egerton, *Ultramicroscopy* 5 (1980) 521.
- [38] R.F. Egerton, P.A. Crozier, P. Rice, *Ultramicroscopy* 23 (1987) 305.
- [39] M. Isaacson, *Physical Aspects of Electron Microscopy and Microbeam Analysis*, in: R. Siegal, R. Beaman (Eds.), Wiley, New York, 1975, Chapter 14.
- [40] S.M. Salihi, V.E. Cosslett, *Philosophical Magazine* 30 (1974) 225.
- [41] J.R. Fryer, F. Holland, *Proceedings of the Royal Society A* 393 (1984) 353.
- [42] J.R. Fryer, *Ultramicroscopy* 14 (1984) 227.
- [43] R.F. Egerton, F. Wang, P.A. Crozier, *Microscopy and Microanalysis* 12 (2006) 65.
- [44] D.A. Muller, J. Silcox, *Philosophical Magazine A* 71 (2007) 1375.
- [45] K. Suenaga, M. Tence, C. Mory, C. Colliex, H. Kato, T. Okazaki, H. Shinohara, K. Hirahara, S. Bandow, S. Iijima, *Science* 290 (2000) 2280.
- [46] M.L. Knotek, *Physics Today* 37 (1984) 24.
- [47] M.I. Buckett, J. Strane, D.E. Luzzi, J.P. Phang, W.W. Wessels, L.D. Marks, *Ultramicroscopy* 29 (1989) 217.
- [48] J. Strane, L.D. Marks, D.E. Luzzi, M.I. Buckett, J.P. Zhand, B.W. Wessels, *Ultramicroscopy* 25 (1988) 253.
- [49] I.G. Salisbury, R.S. Timsit, S.D. Berger, C.J. Humphreys, *Applied Physics Letters* 45 (1984) 1289.
- [50] R.S. Payne, G. Beamson, *Polymer* 34 (1993) 362.
- [51] M. Hayashida, T. Kawasaki, Y. Kimura, Y. Takai, *Nuclear Instruments and Methods in Physics Research B* 248 (2006) 273.
- [52] J.R. Fryer, *Ultramicroscopy* 23 (1987) 321.
- [53] A.H. Zewail, J.M. Thomas, *4D Electron Microscopy*, Imperial College Press, London, 2010.
- [54] Y. Murata, J.R. Fryer, T. Baird, H. Murata, *Acta Crystallographica Section A* 39 (1977) 838.
- [55] W.R.K. Clark, J.N. Chapman, A.M. MacLeod, R.P. Ferrier, *Ultramicroscopy* 5 (1980) 195.
- [56] K.H. Downing, R.M. Glaeser, *Ultramicroscopy* 20 (1986) 269.
- [57] P. Bullough, R. Henderson, *Ultramicroscopy* 21 (1987) 223.
- [58] R.M. Glaeser, G. McMullan, A.R. Faruqi, R. Henderson, *Ultramicroscopy* 111 (2011) 90.
- [59] K. Varlot, J.M. Martin, C. Quet, Y. Kihn, *Ultramicroscopy* 68 (1997) 123.
- [60] K. Siangchaew, M. Libera, *Philosophical Magazine A* 80 (2000) 1001.
- [61] C.R. Bradley, N.J. Zaluzec, *Ultramicroscopy* 28 (1989) 335.
- [62] M. Inokuti, *Reviews of Modern Physics* 43 (1970) 297.
- [63] A. Howie, M.N. Mohd Muhid, F.J. Rocca, U. Valdre, *Institute of Physics Conference Series*, Vol. 90, IOP, Amsterdam, 1987, p. 155.
- [64] P. Li, R.F. Egerton, *Ultramicroscopy* 101 (2004) 161.
- [65] M.R. Stevens, Q. Chen, U. Weierstall, J.C.H. Spence, *Microscopy and Microanalysis* 6 (2000) 368.
- [66] R.F. Egerton, *Electron Energy-Loss Spectroscopy in the Electron Microscope*, third ed., Springer, New York, 2011.
- [67] H. Rose, *Ultramicroscopy* 110 (2010) 488.
- [68] U. Kaiser, J. Biskupek, J.C. Meyer, J. Leschner, L. Lechner, H. Rose, M. Stoeger-Pollach, A.N. Khlobystov, P. Hartel, H. Mueller, M. Haider, S. Eyhusen, G. Benner, *Ultramicroscopy* 111 (2011) 1239.
- [69] Y. Beyer, R. Beanland, P.A. Midgley, *Micron* 43 (2012) 428.
- [70] D. Van Dyck, *Ultramicroscopy* 110 (2010) 571.